SPECIAL
Global Precipitation Measurement (GPM)
COLLECTION

Oceanic Validation of IMERG-GMI Version 6 Precipitation Using the GPM Validation Network

DANIEL C. WATTERS,[a] PATRICK N. GATLIN,[b] DAVID T. BOLVIN,[c,d] GEORGE J. HUFFMAN,[c] ROBERT JOYCE,[c,d] PIERRE KIRSTETTER,[e,f,g,h] ERIC J. NELKIN,[c,d] SARAH RINGERUD,[c] JACKSON TAN,[c,i] JIANXIN WANG,[c,d] AND DAVID WOLFF[j]

[a] *NASA Postdoctoral Program, NASA Marshall Space Flight Center, Huntsville, Alabama*
[b] *NASA Marshall Space Flight Center, Huntsville, Alabama*
[c] *NASA Goddard Space Flight Center, Greenbelt, Maryland*
[d] *Science Systems and Applications, Inc., Lanham, Maryland*
[e] *Advanced Radar Research Center, University of Oklahoma, Norman, Oklahoma*
[f] *School of Civil Engineering and Environmental Sciences, University of Oklahoma, Norman, Oklahoma*
[g] *School of Meteorology, University of Oklahoma, Norman, Oklahoma*
[h] *NOAA/National Severe Storms Laboratory, Norman, Oklahoma*
[i] *University of Maryland, Baltimore County, Baltimore, Maryland*
[j] *NASA Wallops Flight Facility, Wallops Island, Virginia*

(Manuscript received 10 August 2023, in final form 26 October 2023, accepted 27 October 2023)

ABSTRACT: NASA's multisatellite precipitation product from the Global Precipitation Measurement (GPM) mission, the Integrated Multi-satellitE Retrievals for GPM (IMERG) product, is validated over tropical and high-latitude oceans from June 2014 to August 2021. This oceanic study uses the GPM Validation Network's island-based radars to assess IMERG when the GPM *Core Observatory*'s Microwave Imager (GMI) observes precipitation at these sites (i.e., IMERG-GMI). Error tracing from the Level 3 (gridded) IMERG V06B product back through to the input Level 2 (satellite footprint) Goddard Profiling Algorithm GMI V05 climate (GPROF-CLIM) product quantifies the errors separately associated with each step in the gridding and calibration of the estimates from GPROF-CLIM to IMERG-GMI. Mean relative bias results indicate that IMERG-GMI V06B overestimates Alaskan high-latitude oceanic precipitation by +147% and tropical oceanic precipitation by +12% with respect to surface radars. GPROF-CLIM V05 overestimates Alaskan oceanic precipitation by +15%, showing that the IMERG algorithm's calibration adjustments to the input GPROF-CLIM precipitation estimates increase the mean relative bias in this region. In contrast, IMERG adjustments are minimal over tropical waters with GPROF-CLIM overestimating oceanic precipitation by +14%. This study discovered that the IMERG V06B gridding process incorrectly geolocated GPROF-CLIM V05 precipitation estimates by 0.1° eastward in the latitude band 75°N–75°S, which has been rectified in the IMERG V07 algorithm. Correcting for the geolocation error in IMERG-GMI V06B improved oceanic statistics, with improvements greater in tropical waters than Alaskan waters. This error tracing approach enables a high-precision diagnosis of how different IMERG algorithm steps contribute to and mitigate errors, demonstrating the importance of collaboration between evaluation studies and algorithm developers.

SIGNIFICANCE STATEMENT: Evaluation of IMERG's oceanic performance is very limited to date. This study uses the GPM Validation Network to conduct the first extensive assessment of IMERG V06B at its native resolution over both high-latitude and tropical oceans, and traces errors in IMERG-GMI back through to the input GPROF-CLIM GMI product. IMERG-GMI overestimates tropical oceanic precipitation (+12%) and strongly overestimates Alaskan oceanic precipitation (+147%) with respect to the island-based radars studied. IMERG's GMI estimates are assessed as these should be the optimal estimates within the multisatellite product due to the GMI's status as calibrator of the GPM passive microwave constellation.

KEYWORDS: Ocean; Precipitation; Algorithms; Microwave observations; Radars/Radar observations; Satellite observations

1. Introduction

Precipitation is critical to the Earth system by acting as a link between the water cycle and energy budget. Observing the transportation of water from the atmosphere to the surface via precipitation is important for natural disaster tracking and mitigation, drought monitoring and agricultural planning

Denotes content that is immediately available upon publication as open access.

Corresponding author: Daniel C. Watters, daniel.c.watters@nasa.gov

DOI: 10.1175/JHM-D-23-0134.1

among a multitude of other reasons. NASA and JAXA have advanced the effort to observe precipitation from a spaceborne vantage with the Tropical Rainfall Measuring Mission (TRMM; 1997–2014) (Simpson et al. 1996; Kummerow et al. 1998) and the Global Precipitation Measurement (GPM) mission (2014–present) (Hou et al. 2014; Skofronick-Jackson et al. 2017; Kidd et al. 2020; Watters and Battaglia 2021a,b). The core satellite of both missions hosted the most advanced spaceborne radar and passive microwave (PMW) radiometer in their respective eras to support our understanding and quantification of global precipitation. In the present era, the GPM *Core Observatory* (CO) hosts the Dual-Frequency Precipitation Radar (DPR), the first and presently only civilian multifrequency precipitation radar in space that is capable of sensing swath precipitation at differing heights throughout the vertical column (Iguchi et al. 2018), and the GPM Microwave Imager (GMI), which observes the total column water content and is the calibration standard for the other PMW radiometers in the GPM constellation provided by other international agencies (Berg et al. 2016). For observing global precipitation on subdaily time scales from space, PMW radiometers are favored as 1) there are presently 11 in space (as of July 2023) that all traverse different low-Earth orbits in comparison to one precipitation radar; 2) PMW radiometers have wider swaths than the DPR (e.g., GMI: 885 km; DPR: 245 km). Consequently, the GPM and TRMM satellite constellations of PMW radiometers underpin NASA's global-gridded precipitation product, the Integrated Multi-satellitE Retrievals for GPM product (IMERG; Huffman et al. 2019b). The GPM PMW constellation samples 90% of Earth's surface within 3 h (Hou et al. 2014), so the IMERG algorithm extends the spatial coverage of the PMW precipitation retrievals via spatiotemporal interpolation, supplemented by lower-quality spaceborne IR estimates, to provide global precipitation estimates at high spatiotemporal resolution (0.1°, 30 min). The IMERG Version 6B (V06B) record covers a 20+-yr period with three different latency runs aimed at disaster response (Early), agricultural modeling and public health applications (Late), and research (Final; Kirschbaum et al. 2017). Consequently, IMERG lends itself to a wide variety of research and applications, including for input to flood, fire and disease exposure forecasts (Kirschbaum et al. 2017; Skofronick-Jackson et al. 2017, 2018), hurricane analyses (Watters and Battaglia 2021b; Petersen et al. 2020), diurnal cycle investigations (O and Kirstetter 2018; Watters and Battaglia 2019; Battaglia et al. 2019; Tan et al. 2019a; Hayden and Liu 2021; Hayden et al. 2023), and climate model evaluations (Watters et al. 2021), among others.

As the most popular precipitation product of the GPM mission (Portier et al. 2023), validating IMERG is of paramount importance for understanding and addressing estimation errors both for algorithm improvements and for alerting the scientific and application communities to product limitations. For instance, Rajagopal et al. (2021) validated IMERG V06B and showed that locations and times without PMW observations have a higher (lower) frequency of light (heavy) precipitation rates due to propagation and morphing artifacts and the limitations of the motion vectors; this led to the development of a scheme to restore the distribution of averaged precipitation fields [Scheme for Histogram Adjustment with Ranked Precipitation Estimates in the Neighborhood (SHARPEN); Tan et al. 2021] to mitigate these errors, which is implemented in IMERG Version 7 (V07). Many IMERG V06 validation studies have been conducted with gauge networks and/or gauge-adjusted ground-radar networks over land, including regions such as the contiguous United States (CONUS; Kirstetter et al. 2020; Huffman et al. 2020a; Wang et al. 2021), Alaska (Gowan and Horel 2020), Europe (Navarro et al. 2019; Tapiador et al. 2020), Brazil (Nascimento et al. 2021), China (Li et al. 2021), Africa (Maranan et al. 2020), the Netherlands (Bogerd et al. 2021), Finland (Mahmoud et al. 2021), Malaysia and the Philippines (Da Silva et al. 2021), and South Korea (Wang et al. 2020). Highlighted IMERG performance issues over land include overestimation of drizzle and underestimation of heavy precipitation (Tan et al. 2016; O et al. 2017; Maranan et al. 2020; Kirstetter et al. 2020; Da Silva et al. 2021), underestimation of orographic precipitation and poor coastal performance (Ramsauer et al. 2018; Navarro et al. 2019; Tapiador et al. 2020; Derin et al. 2021, 2022; Derin and Kirstetter 2022), and varying performance by satellite sensor type (Tan et al. 2016; Kirstetter et al. 2020; Petersen et al. 2020; Derin et al. 2021, 2022; You et al. 2021).

While oceanic precipitation accounts for ~78% of the global occurrence (Trenberth et al. 2007), our understanding of IMERG performance over ocean is limited to date. Evaluating any satellite precipitation product over ocean is challenging as ground-based precipitation measurements are notoriously difficult to obtain from the ocean surface and hence are scarce. Previous evaluations have used the limited oceanic surface precipitation measurements provided by ship- and buoy-based in situ instruments, as well as ground-based radars and gauges located on islands or close to coastlines. Wang et al. (2022) evaluated the IMERG Final Run product at its native spatiotemporal resolution against an S-band weather radar covering the waters surrounding Kwajalein between 2014 and 2018; they identified IMERG V05 and V06 to underestimate oceanic precipitation. However, the underestimation by V06 is much reduced thanks to a lower systematic bias, improved precipitation detectability and upgraded morphing. Bolvin et al. (2021) compared the IMERG V06B Final Run monthly estimates to 37 Pacific Ocean atolls across a 20-yr period, identifying IMERG to underestimate light precipitation (<3 mm day^{-1}) and overestimate heavy precipitation (>17 mm day^{-1}) which drives an overall overestimation bias of +0.67%. Derin et al. (2021, 2022) evaluated IMERG V06B precipitation detection and quantification across the land–coast–ocean continuum for the CONUS using the Ground Validation Multi Radar Multi Sensor (GV-MRMS) product derived from the CONUS radar network; they identified greater IMERG detection over ocean while false alarms affect oceanic performance. Other studies have considered IMERG's oceanic performance relative to references such as shipboard disdrometers, the GPM-CO's DPR (Khan and Maggioni 2019), moored buoys (Prakash et al. 2018), and passive aquatic listeners (Bytheway et al. 2023).

An improved understanding of IMERG's ability to capture oceanic precipitation is of paramount importance, with assessments over multiple years and multiple oceanic sites necessary. The GPM Validation Network (VN; Gatlin et al. 2020), a software system run at NASA Marshall Space Flight Center,

provides an opportunity to conduct extensive oceanic validation of IMERG. The GPM VN geometrically matches precipitation retrievals from the GPM-CO sensors [i.e., DPR, CORRA (Combined DPR-GMI), and GPROF (Goddard Profiling Algorithm)] to 118 ground-based radars (GRs), including six island-based radars located across Alaska, Hawaii, Puerto Rico, Guam, and Kwajalein. The GPROF footprint-scale precipitation estimates, retrieved from GPM constellation measurements via a Bayesian scheme which uses GPM-CO DPR and GMI observations as a retrieval database (Kummerow et al. 2015; Randel et al. 2020), are gridded in the first step of the IMERG algorithm. Consequently, the VN's GR-to-GPROF GMI matchups can be gridded to validate IMERG against the GR data, and enable error tracing from IMERG-GMI (i.e., IMERG at instances of GMI overpasses) back through to the input GPROF-GMI product.

In this study, we conduct an extensive validation of IMERG-GMI V06B over tropical and high-latitude oceans using the GPM VN. IMERG-GMI is assessed across the GPM era in the period June 2014–August 2021. Novelties of this study include assessing IMERG's oceanic precipitation performance using multiple island-based radar sites across a 7+-yr period, and tracing errors in IMERG back through to the source GPROF product at instances of GPM-CO GMI overpasses. IMERG and GPROF GMI data are compared to the GR data at the 30-min, 0.1° × 0.1° IMERG native grid resolution, unlike other studies which typically validate IMERG at coarser resolutions (Pradhan et al. 2022). IMERG-GMI performance is assessed by statistical analysis, precipitation distribution, and as a function of precipitation intensity. While IMERG is a multisatellite product, we only consider IMERG performance for the GMI sensor for two reasons: 1) the GMI is the calibration standard and most accurate of the GPM constellation of PMW radiometers (Berg et al. 2016; Wentz and Draper 2016; Skofronick-Jackson et al. 2018), and hence should provide the best performance within IMERG, and 2) the GPM VN currently produces matchups with the GPM-CO sensors alone, hence this analysis is only possible with the GMI at present. We assess IMERG-GMI V06B upon the release of V07 because of the lack of knowledge of IMERG V06B oceanic performance, and to allow us to track the impact of extensive changes in V07 (e.g., the introduction of the SHARPEN scheme). This validation study is designed to further our understanding of how to improve the IMERG algorithm for oceanic precipitation, as well as to understand how IMERG-GMI is impacted by the performance of the source GPROF data.

2. Data

In this IMERG validation study, we use three different GPM data products: the Level 3 IMERG V06B Final Run product, the Level 2 GPROF V05 climate product, and the Level 2 GRtoGPROF V2.3 product from the GPM Validation Network. Note that GPROF V05 products are used in the GPM V06 product suite.

a. IMERG V06B final run

IMERG is a Level 3 (gridded) global precipitation product, with spatial and temporal resolutions of 0.1° and 30 min, respectively (Huffman et al. 2019b, 2020b). The IMERG V06B Final Run data are available from June 2000 to September 2021 (Huffman et al. 2019a). The Final Run of IMERG is selected for this study as we want to assess the research-level estimates (with a 3.5-month latency), which are considered the best of all runs due to the inclusion of gauge analyses (although no gauges provide data in the oceanic regions studied herein), and the use of all available satellite data and the most extensive algorithm techniques.

The IMERG V06B algorithm principally intercalibrates, merges and interpolates the GPM PMW satellite constellation's precipitation estimates; the PMW constellation satellites all operate in low-Earth orbits, and IR-based precipitation estimates from geostationary satellites are used to aid in covering PMW-sparse regions/times. PMW retrievals typically have more skill in representing precipitation than IR retrievals (Kirstetter et al. 2020; Petersen et al. 2020), as PMW radiometers are sensitive to precipitating hydrometeors in the atmospheric column, unlike IR sensors which are limited to cloud top measurements. Consequently, PMW retrievals are favored over IR retrievals where both are available.

The IMERG V06B Final Run algorithm has five key steps:

1) PMW gridding: Gridding and combining the PMW constellation precipitation estimates which are principally produced using the Goddard Profiling V05 algorithm (GPROF; Kummerow et al. 2015; Randel et al. 2020). Note that the IMERG V06B gridder is subject to an error which incorrectly geolocates the PMW footprint estimates by 0.1° eastward, and the gridded CORRA calibrations by 0.025° eastward, globally between 75°N and 75°S; this is referred to as the geolocation error/offset henceforth and discussed below.
2) PMW calibration: Intercalibration of the gridded PMW estimates to the GPM-CO/TRMM Combined Radar-Radiometer V06 estimates (CORRA; Olson 2022), which first are climatologically adjusted to the Global Precipitation Climatology Project satellite–gauge V2.3 product (GPCP; Adler et al. 2003, 2018) to compensate for CORRA biases over high-latitude ocean (where CORRA underestimates precipitation) and over land (where CORRA overestimates precipitation; Huffman et al. 2020a). The CORRA intercalibration of the GMI/TRMM Microwave Imager (TMI) operates on a dynamic rolling 9-pentad basis via the quantile–quantile matching technique, with the constellation satellites climatologically calibrated via a quantile–quantile fit to the GMI/TMI.
3) PMW propagation: The calibrated, gridded 30-min PMW estimates are propagated forward and backward in time using numerical model-derived motion vectors of total column water vapor (Tan et al. 2019b), followed by quasi-Lagrangian temporal linear interpolation (morphing; Joyce et al. 2004; Joyce and Xie 2011) to increase the spatial coverage of the low-Earth-orbit PMW sampling.
4) Kalman filter merging: Merging at each 0.1° grid box of the forward-propagated PMW estimates, the backward-propagated PMW estimates, and the PMW-calibrated precipitation estimates from geostationary IR satellites via a Kalman filter.

5) Gauge calibration: Calibration of the merged PMW-IR half-hour gridded estimates at the monthly scale to the gauge-based, undercatch-adjusted Global Precipitation Climatology Centre (GPCC; Schneider et al. 2014) Full/Monitoring product over land. Note that the gauge analyses do not contribute to the oceanic regions in IMERG.

A geolocation offset was identified in the IMERG V06B gridder in the latitude range 75°N–75°S during this study, specifically a shift by one 0.1° grid box to the east. Computations using IMERG V06B (and all earlier versions) are affected by this error, most acutely for studies that depend on data at the native 0.1° spatial resolution. The present study assesses the impact of the gridder geolocation error and quantifies the effect over selected oceanic regions in section 4.

In the IMERG product data files, three different precipitation estimates are provided at different steps in the algorithm. The HQprecipitation variable provides the CORRA-calibrated gridded PMW estimates (step 2 of 5), with the HQprecipSource variable detailing which PMW constellation radiometer provided the HQprecipitation estimate. The precipitationUncal variable provides the merged PMW-IR gridded estimates prior to gauge calibration (step 4 of 5), and the precipitationCal variable is the final IMERG estimate which adds gauge calibration over land to precipitationUncal (step 5 of 5).

b. *GPROF V05 climate product*

GPROF (NASA 2022; Kummerow et al. 2015; Randel et al. 2020) is a Level 2 (instantaneous footprint) global precipitation product. For the GMI sensor, GPROF has a spatial resolution at the scale of the 18.7 GHz field of view (10.9 km × 18.1 km; C. Kummerow 2022, personal communication). The GPROF V05 climate data for the GMI sensor, referred to as GPROF-CLIM in this paper, are available from March 2014 to January 2022 (Kummerow 2017). GPROF-CLIM is selected because it is the GPROF product ingested in the IMERG Final Run algorithm's first step (PMW gridding). GPROF-CLIM differs from the near-real-time and research-level GPROF products by using ECMWF reanalysis (ERA-Interim) data as an ancillary input to constrain the retrieval; these data are only available approximately 3 months after the satellite observations, with the other GPROF products using the Japanese Global Analysis (GANAL) model data instead to satisfy shorter latencies of less than 2 days.

The GPROF algorithm is a parametric Bayesian algorithm which retrieves precipitation estimates, based on brightness temperature measurements at different frequencies, from each PMW radiometer in the GPM constellation. GPROF works on the principle that CORRA V04 precipitation profiles retrieved from coincident GPM-CO DPR and GMI observations can be used to create an a priori database to aid in constraining precipitation retrievals from the GMI and other PMW constellation members. Bayesian techniques are used to retrieve a weighted mean of precipitation profiles from the a priori database that corresponds to the observed channel brightness temperatures. The contributing weight of each precipitation profile is determined by the difference between the observed and associated brightness temperatures for each radiometrically consistent precipitation profile, the instrument error, and the sensitivity of each frequency as a function of surface type. Ancillary data from ECMWF's ERA-Interim reanalysis are used to constrain the retrieval from the a priori database and subset it by 2-m temperature, total column water vapor, and land surface classification.

GPROF's instantaneous surface precipitation rate variable, surfacePrecipitation, is used in this analysis.

c. *GRtoGPROF V2.3*

The GPM Validation Network's Ground Radar to GPROF (GRtoGPROF) V2.3 product is a Level 2 (instantaneous footprint) precipitation product that covers a 125-km radius centered on a ground-based radar site. The GRtoGPROF product spatially collocates the GR retrievals to the GMI footprint scale used in GPROF (10.9 km × 18.1 km) to allow for direct comparison between the two products at a consistent resolution. GR variables such as precipitation, radar reflectivity factor, hydrometeor identification and dual-polarization fields are provided at this GPROF-GMI resolution at each GR scan elevation along the vertical profile normal to the surface and along the GMI line-of-sight slant path (as the GMI is a conically scanning sensor; see Fig. 5.4-1 of NASA-GSFC 2015). The VN's GRs mostly operate at S-band frequency (~2.8 GHz). The VN V2.3 data are available from March 2014 to December 2022 (NASA 2023).

The workflow of the GPM VN is described in detail by Gatlin et al. (2020), NASA-GSFC (2015), and Schwaller and Morris (2011). The GPM VN ingests ground-based polarimetric radar data from 118 research and operational sites principally located across CONUS, Alaska, Hawaii, Pacific islands, and Brazil. These high-quality polarimetric GR data are subject to operational processing, including quality control and calibration procedures, and product generation, including precipitation and hydrometeor identification retrievals (Pippitt et al. 2015). Subsequently, the VN only produces GRtoGPROF matchups in cases where there is sufficient precipitation within the ground radar's vicinity; specifically, a GPM-CO overpass event must have ≥20 DPR precipitating pixels (gridded to 4 km × 4 km) within 100 km of the ground radar for the matchup product to be generated. Furthermore, the ground radar scans selected for the matchups are those for which the lowest elevation scan start time is within ±5 min of the GPM-CO ground track falling within the ground radar vicinity.

The Colorado State University Hydrometeor Identification Rainfall Optimization (CSU-HIDRO) precipitation rate retrieval (GR_RC_rainrate_VPR; Cifelli et al. 2011) is used for this analysis because it selects the most appropriate polarimetric rainfall estimator based on the polarimetric measurements of the precipitation field. Only near-surface precipitation rates from the lowest elevation scan (0.5°) are used in this analysis. Note that the CSU-HIDRO algorithm does not produce precipitation rate retrievals for ice-phase precipitation. The VN only includes GR precipitation rates in the range $0.01 \leq R \leq 300$ mm h^{-1} when spatially matching to the GPROF-GMI footprint size, therefore regions of no rain are not included in the resolution matching procedure and a conditional

precipitation rate is computed; alternatively, IMERG and GPROF-CLIM retrieve unconditional precipitation rates, i.e., these satellite algorithms incorporate rain and no rain within the footprint grid box. Freezing level information is used in this analysis, which the VN acquires from the 6-hourly model analyses of the National Oceanic and Atmospheric Administration (NOAA) Global Forecast System for matchup regions outside of CONUS.

3. Methodology

Gridded oceanic precipitation rates from IMERG-GMI and GPROF-CLIM are validated against those from VN GRs across tropical and high-latitude island sites (Fig. 1). The tropical island sites include Hawaii's Kauai (PHKI) and Molokai (PHMO) islands, Puerto Rico (TJUA), Guam (PGUA), and the Kwajalein Atoll (KWAJ), while the high-latitude island site is Alaska's Middleton Island (PAIH). The satellite precipitation products are compared to the GRs where the GPM-CO's GMI measures within the GR vicinity (125-km radius) and sufficient surface precipitation is identified by the DPR. The analysis period covers all GMI precipitating overpass events within the period June 2014–August 2021.

a. *Gridding process*

GR and GPROF-CLIM precipitation estimates at the GPROF-GMI footprint scale are gridded at the IMERG native resolution 0.1° × 0.1° using the backward gridding technique applied by IMERG (Figs. 2a–d). The backward gridding technique maps a grid box on a cylindrical equidistant grid (75°N–75°S latitudinal range) with the satellite footprint value that has the minimum squared elliptical distance between the footprint center and the grid box center. All gridded precipitation rates are rounded to two decimal places, and precipitation rates below the IMERG rain–no rain threshold of 0.03 mm h^{-1} are set to zero to match the IMERG V06B algorithm.

Other geophysical variables from the GRtoGPROF product are gridded using the fine/average technique instead. This technique maps the geophysical variable to a 0.025° × 0.025° cylindrical equidistant grid using nearest neighbor interpolation, then averages the 16 fine-scale grid boxes within a single 0.1° × 0.1° grid box. This averaging can take two forms: 1) mean or 2) mode. The mode is used for deducing the most commonly occurring hydrometeor identification (HID), and GR bin-top and -bottom heights, while the mean is used for determining the percentage of GR native-resolution precipitating bins within a grid box.

The backward gridding technique is used for gridding precipitation estimates in this analysis to enable error tracing through the IMERG algorithm back to the input GPROF-CLIM footprints. Alternatively, the fine/average gridding technique is used for other geophysical variables (e.g., mode HID) as it allows for multiple satellite footprints to contribute to one grid box in a weighted fashion, and hence should better represent the spatial distribution within the grid box.

b. *Error tracing from GPROF to IMERG*

A novel goal of our study is to trace errors from GPROF through the IMERG algorithm at instances of GMI overpasses. By focusing on errors at the inception of the IMERG algorithm, we can both determine the strength of IMERG's performance over ocean and determine the algorithm steps that lead to improvements or deteriorations. By gridding the GPROF-CLIM footprints using IMERG's backward gridding technique, we can conduct a thorough error tracing analysis (Fig. 2). The key error tracing steps in the analysis are as follows:

1) GPROF-CLIM V05: The GPROF-CLIM GMI V05 precipitation rates at the footprint scale subject to the IMERG backward gridding technique. Note that these gridded estimates are not subjected to the geolocation error in IMERG V06B (discussed in section 2a).
2) IMERG-GMI V06B [PMW]: The output of step 1 in the IMERG algorithm (PMW gridding). The same as the gridded GPROF-CLIM V05 description, except that this PMW gridding is subject to IMERG V06's geolocation error whereby the footprint estimates are assigned to the grid box 0.1° eastward of where they are located.
3) IMERG-GMI V06B [PMW + CORRA Cal.]: The output of step 2 in the IMERG algorithm (PMW calibration). The same as IMERG V06B [PMW], except that the gridded GMI estimates are now subject to CORRA V06 intercalibration (and in turn, GPCP V2.3 climatological adjustment).
4) IMERG-GMI V06B [PMW + CORRA Cal.]–Offset Corrected: The output of step 2 in the IMERG algorithm (PMW calibration), except with the geolocation offset corrected by shifting the grid box values back 0.1° westward. Note that while we correct for the PMW geolocation offset, we cannot correct for the CORRA calibration geolocation offset by 0.025° eastward as it is entangled within the algorithm, though the IMERG algorithm team expects the impact of this to be minimal.

For an IMERG GMI-only oceanic analysis such as this, the output of step 2 of the IMERG V06B algorithm is the same as the final output in step 5 of the algorithm (section 2a); this is because V06B GMI oceanic grid boxes are not subject to PMW propagation, Kalman filter merging, or gauge calibration as there are no precipitation gauges used by IMERG in the selected island regions. Consequently, errors can be attributed to the PMW gridding geolocation offset and CORRA calibration components of the IMERG V06B algorithm.

Figure 2 showcases how the GR and GPROF-CLIM footprints are gridded to the IMERG grid to enable the validation process. Furthermore, the error tracing process is highlighted by comparing each precipitation variable from GPROF-CLIM through to IMERG to the GR.

c. *Validation statistics*

Grid boxes are only analyzed if the GR and satellite precipitation rates are above the IMERG rain–no rain threshold of 0.03 mm h^{-1}; consequently, the sample size can differ between each of the error tracing steps. Furthermore, to ensure that only high-quality GR grid box estimates contribute to this

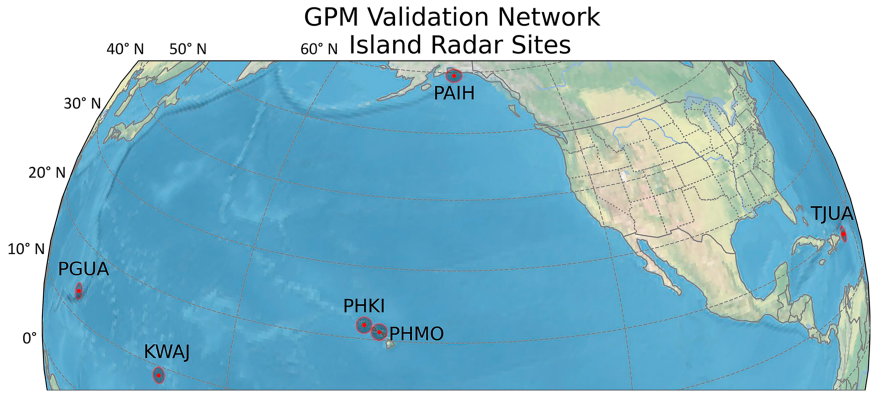

FIG. 1. The GPM Validation Network's island-based radar sites used in this study: Alaska's Middleton Island (PAIH; 59.5°N, 146.3°W), Hawaii's Kauai (PHKI; 21.9°N, 159.6°W) and Molokai (PHMO; 21.1°N, 157.2°W) islands, Puerto Rico (TJUA; 18.1°N, 66.1°W), Guam (PGUA; 13.5°N, 144.8°E), and the Kwajalein Atoll (KWAJ; 8.7°N, 167.7°E). Points represent the radar locations, while the surrounding shaded circles represent 125-km range from the respective radar. These sites provide satellite matchups throughout the GPM era.

analysis, a GR estimate at 0.1° × 0.1° is considered only if at least half of the native-resolution GR bins within are precipitating. The analysis is restricted to liquid precipitation alone by using two conditions: 1) only grid boxes where the mode GR bin height is more than 1 km below the freezing level are analyzed; 2) grid boxes which are dominated by ice-phase precipitation according to the GR are excluded.

A variety of statistical measures are used to quantify the performance of each of the satellite products. Systematic errors in the satellite products are determined using the normalized mean relative bias:

$$\text{mean relative bias (\%)} = \frac{\sum_{i=1}^{N} \Delta R_i}{\sum_{i=1}^{N} R_{\text{GR},i}} \times 100\%, \quad (1)$$

and the normalized mean absolute bias:

$$\text{mean absolute bias (\%)} = \frac{\sum_{i=1}^{N} |\Delta R_i|}{\sum_{i=1}^{N} R_{\text{GR},i}} \times 100\%, \quad (2)$$

where N is the grid box sample size, i is the grid box index, $R_{\text{SAT},i}$ and $R_{\text{GR},i}$ are the precipitation rates for the satellite and GR products for grid box i, respectively, and $\Delta R_i = R_{\text{SAT},i} - R_{\text{GR},i}$. Absolute random errors are quantified by the random error statistic:

$$\text{random error (\%)} = \frac{\sum_{i=1}^{N} |\Delta R_i - \overline{\Delta R_i}|}{\sum_{i=1}^{N} R_{\text{GR},i}} \times 100\%, \quad (3)$$

and the standard deviation:

$$\text{standard deviation (\%)} = \frac{\sqrt{\sum_{i=1}^{N} (\Delta R_i - \overline{\Delta R_i})^2}}{\overline{R_{\text{GR}}}} \times 100\%, \quad (4)$$

where $\overline{\Delta R_i} = \left(\sum_{i=1}^{N} \Delta R_i\right)/N$ and $\overline{R_{\text{GR}}} = \left(\sum_{i=1}^{N} R_{\text{GR},i}\right)/N$. The optimal value of these statistics is 0%. The Pearson correlation coefficient for precipitation rates between each of the satellite products and the GR is also determined to assess the strength of their linear relationship. The optimal value of the correlation coefficient is 1. Tropical oceanic statistics are determined from all grid boxes across the five tropical radar sites.

4. Results

a. Statistical analysis

Density scatterplots for IMERG-GMI and GPROF-CLIM performance against GR precipitation retrievals over high-latitude and tropical oceans are shown in Figs. 3 and 4, respectively. The corresponding validation statistics are detailed in Table 1. The error tracing in the density scatterplots can be understood as follows: IMERG-GMI [PMW] is the same as GPROF-CLIM though with a 0.1° eastward offset in the data that is an innate inaccuracy in the IMERG V06B gridder (discussed in section 2a), IMERG [PMW + CORRA Cal.] adds CORRA calibration effects to IMERG-GMI [PMW] and is still subject to the geolocation offset, and IMERG-GMI [PMW + CORRA Cal.]–Offset Corrected showcases the impact if IMERG V06B were to have correctly geolocated the IMERG-GMI [PMW + CORRA Cal.] data. IMERG-GMI [PMW + CORRA Cal.] can be considered the final output from IMERG V06B for GMI overpasses over ocean, as the IMERG-GMI [Uncal] and IMERG-GMI [Cal] variables from later in the algorithm have identical statistics.

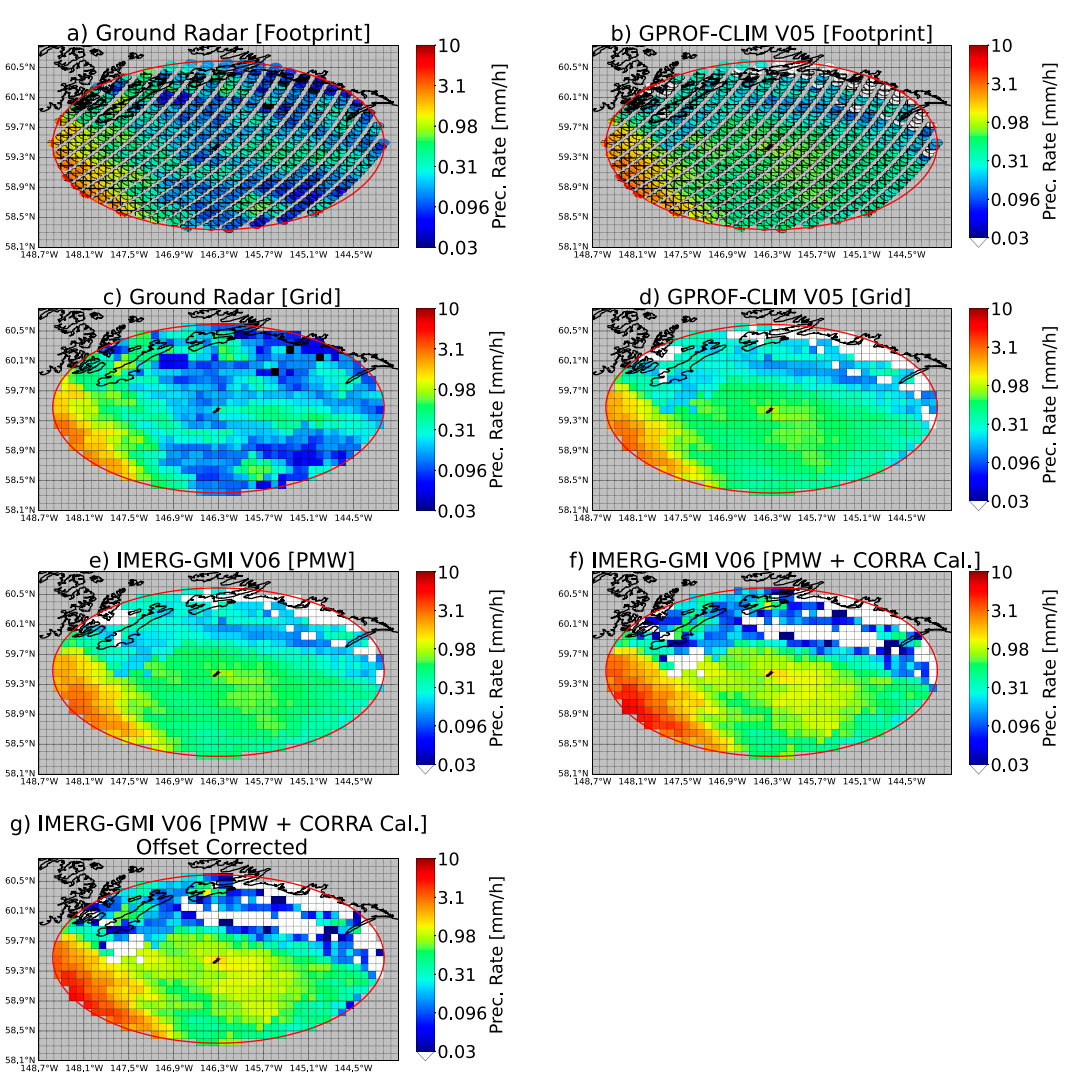

FIG. 2. A precipitation case study when the GPM-CO orbited over Alaska's Middleton Island on 19 Jul 2017 (ground radar site PAIH; GPM granule 19256). Surface precipitation rates at the GPROF-GMI footprint scale (10.9 km × 18.1 km) from (a) the ground radar and (b) GPROF-CLIM V05, and at the IMERG 0.1° × 0.1° grid scale from (c) the ground radar, (d) GPROF-CLIM V05, and IMERG V06B's (e) microwave-only, (f) microwave with CORRA V06 calibration, and (g) microwave with CORRA V06 calibration and the V06B geolocation offset corrected (discussed in section 2a). The GMI measurements are from 0957:10 to 0957:44, the IMERG-GMI data represents the half hour 0930:00–0959:59, and the ground radar's lowest elevation scan started at 0955:45. GR precipitation rates < 0.01 mm h^{-1} are set to black as they cannot be quantified due to the sensitivity of the GR.

The results highlight a tendency for GPROF-CLIM to outperform IMERG-GMI over both high-latitude and tropical oceans, with the IMERG estimate as gridded and calibrated in V06B generally having the worst statistics (Table 1). Over the high-latitude ocean, IMERG-GMI exhibits much worse statistics than GPROF-CLIM. IMERG-GMI increases the mean relative bias from +15% for the input GPROF-CLIM data to +147%, increases the random error from 41% to 154% and decreases the correlation from 0.85 to 0.75. When corrected for the geolocation offset, the statistics only slightly improve, with the bias decreasing from +147% to +145%, the random error decreasing from 154% to 147%, and the correlation increasing from 0.75 to 0.79. The impact of the CORRA calibration to the GPROF-CLIM data is depicted by a shift in the density scatterplot's modal concentration from the 1:1 line, a conditional bias in the quantile–quantile line into the satellite domain, and a larger spread in the density scatterplot along the satellite (y) axis (Fig. 3). Contrasting the impact of the offset for both the uncalibrated and calibrated estimates, the absence of the offset leads to marginally

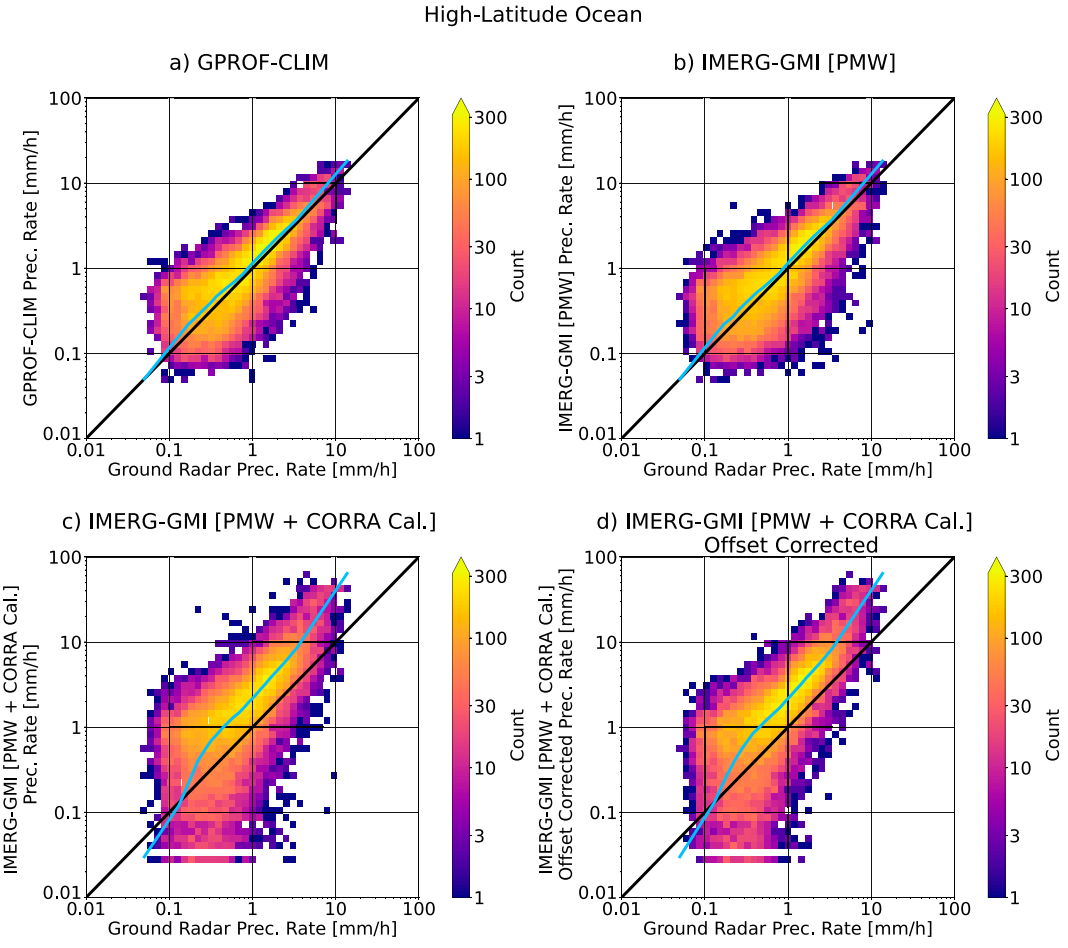

FIG. 3. Density scatterplots of 0.1° × 0.1° gridded precipitation retrievals from IMERG V06B Final Run and GPROF-CLIM V05 vs the reference GR over the high-latitude ocean. The IMERG error tracing variables include (a) GPROF-CLIM gridded, (b) IMERG's PMW (i.e., GPROF-CLIM gridded with 0.1° offset eastward), (c) IMERG's PMW subject to CORRA calibration (including the 0.1° offset eastward), and (d) IMERG's PMW subject to CORRA calibration with the geolocation offset corrected. Results are restricted to GMI overpasses of the GRs in the period June 2014–August 2021 only. The 1:1 line and quantile–quantile line are black and blue, respectively.

better bias values and moderately improved deviation and correlation values. The high-latitude ocean results highlight that the largest difference in IMERG-GMI performance arises from the CORRA calibration, which can be traced to the GPCP climatological adjustment (see section 5 and Fig. 9).

By contrast, IMERG-GMI exhibits similar statistics to its input GPROF-CLIM data over the tropical ocean, with only a minor degradation in all statistics (excluding correlation) due to the IMERG algorithm (Table 1). IMERG-GMI increases the random error from 71% for GPROF-CLIM to 92% and decreases the correlation from 0.61 to 0.42. While IMERG-GMI slightly improves the mean relative bias from +14% for GPROF-CLIM to +12%, it increases the mean absolute bias from 73% to 92% because of a larger deviation which stays centered close to the 1:1 line (Figs. 4a,c). When the geolocation offset is corrected, the statistics are close to those for the input GPROF-CLIM data and improve upon those when the offset is present. For instance, the IMERG-GMI data with the offset corrected have an improved mean absolute bias (74% compared to 92%), random error (73% compared to 92%), and correlation (0.58 compared to 0.42) as opposed to the output IMERG-GMI V06B data which are subject to the offset. This reduction in deviation statistics and improved correlation is evident from the smaller spread in the density scatterplot and higher sample around the 1:1 line (Figs. 4c,d). The validation statistics and density scatterplots show that the geolocation offset has a larger impact on IMERG-GMI performance than the CORRA calibration effects over the tropical ocean, with the reverse true over the high-latitude ocean. Deviation statistics for IMERG-GMI over the tropical ocean are generally better than those over the high-latitude ocean, even though the tropical-ocean density scatterplots show a greater spread, because the high-latitude-ocean density scatterplots have a more significant conditional bias (Figs. 3c,d and 4c,d).

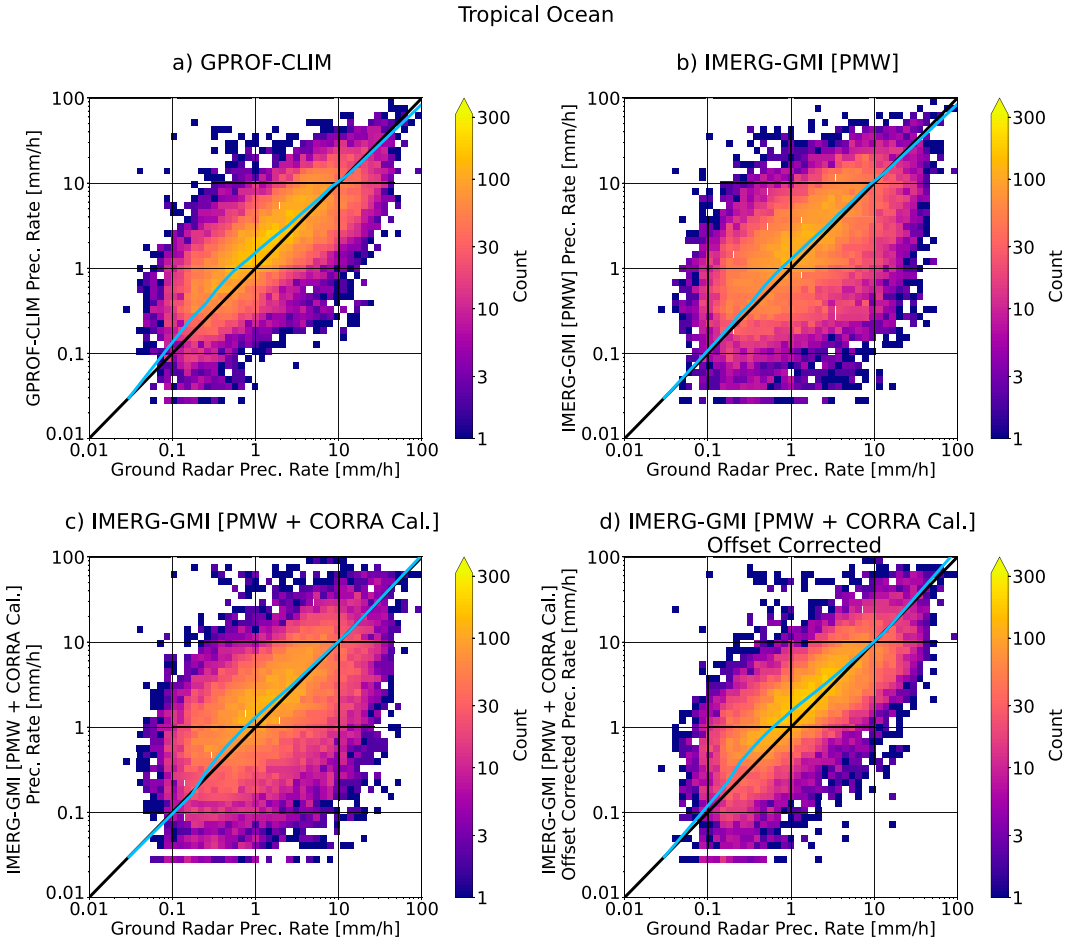

FIG. 4. As in Fig. 3, but for the tropical ocean.

IMERG-GMI performance is generally superior over the tropical ocean to that over the high-latitude ocean. Over the tropical ocean, IMERG-GMI exhibits a smaller overestimated mean relative bias (tropical = +12%; high latitude = +147%) and a smaller random error (tropical = 92%; high latitude = 154%). However, IMERG-GMI exhibits a stronger linear relationship with GR retrievals over the high-latitude ocean than the tropical ocean (tropical = 0.42; high latitude = 0.75). In contrast to IMERG-GMI, GPROF-CLIM performance is generally superior over the high-latitude ocean to that over the tropical ocean, as evidenced by much smaller deviation statistics and a superior correlation coefficient (tropical = 0.61; high latitude = 0.85). However, the small overestimated mean relative bias for GPROF-CLIM over tropical and high-latitude oceans is relatively consistent (tropical = +14%; high latitude = +15%). Large systematic and random errors in IMERG-GMI over the high-latitude ocean are caused by IMERG's CORRA calibration process, which enhances GPROF-CLIM's errors; this unexpectedly shows that IMERG's CORRA calibration process can have a detrimental effect on the accuracy of IMERG-GMI estimates over the Alaskan high-latitude ocean. IMERG V06B's 0.1° geolocation offset error has a larger impact than the CORRA calibration process over the tropical ocean, though the offset error has a relatively small impact compared to the CORRA calibration impact over the high-latitude ocean. The minimal impact of the geolocation offset over the high-latitude ocean compared to the tropical ocean is likely due to the higher prevalence of convection over the tropics, resulting in more spatial and temporal variability in tropical precipitation; however, the 0.1° gridbox offset distance is smaller at Middleton Island (~5.6 km) than in the tropics (~10.3–11.1 km) because as latitude increases, the size of a degree of longitude decreases.

Table 1 restricts the analysis to GPROF-CLIM and the first two steps in the IMERG V06B algorithm (plus a correction for the geolocation offset in the V06B algorithm). The GPROF-CLIM statistics almost identically match those from the research-level GPROF product, and IMERG-GMI [PMW + CORRA Cal.] statistics identically match those from IMERG-GMI [Uncal] and IMERG-GMI [Cal] for the GMI oceanic analysis. Consequently, only the four products/variables in Table 1 are considered henceforth.

b. *Probability density analysis*

The probability and cumulative density functions (PDF and CDF, respectively) for precipitation retrievals from IMERG-

TABLE 1. Validation statistics for IMERG V06B Final Run and GPROF-CLIM V05 against reference GR retrievals over the high-latitude and tropical oceans. Results are restricted to GMI overpasses of the GRs in the period June 2014–August 2021 only. Error tracing variables and analysis statistics are defined in sections 3b and 3c, respectively. Best and worst values for each statistic per region are shown in bold and italic text, respectively.

Oceanic site	Product	Sample	Mean relative bias (%)	Mean absolute bias (%)	Random error (%)	Standard deviation (%)	Correlation
High latitude	GPROF-CLIM	30 658	+**15**	**42**	**41**	**68**	**0.85**
	IMERG-GMI [PMW]	30 431	+**15**	48	47	77	0.81
	IMERG-GMI [PMW + CORRA Cal.]	29 885	*+147*	*159*	*154*	*303*	*0.75*
	IMERG-GMI [PMW + CORRA Cal.]–Offset Corrected	30 179	+145	154	147	293	0.79
Tropics	GPROF-CLIM	28 532	+14	**73**	**71**	**140**	**0.61**
	IMERG-GMI [PMW]	28 080	+**9**	89	89	168	0.45
	IMERG-GMI [PMW + CORRA Cal.]	27 845	+12	*92*	*92*	*190*	*0.42*
	IMERG-GMI [PMW + CORRA Cal.]–Offset Corrected	28 573	*+17*	74	73	159	0.58

GMI, GPROF-CLIM, and GR at the grid box scale over high-latitude and tropical oceans are shown in Figs. 5 and 6. In this section, precipitation rates (R) are defined as light for $R < 0.1$ mm h^{-1}, intermediate for $0.1 \leq R \leq 1$ mm h^{-1}, and heavy for $R > 1$ mm h^{-1}.

For the high-latitude ocean, precipitation occurrence peaks at ~0.07 mm h^{-1} for the GR, while peaking at ~0.2 mm h^{-1} for GPROF-CLIM, and ~0.05 mm h^{-1} for IMERG-GMI (Fig. 5a). The PDF of precipitation volume peaks at ~0.15 mm h^{-1} for the GR, ~0.23 mm h^{-1} for GPROF-CLIM, and ~1.03 mm h^{-1} for IMERG-GMI (Fig. 5b). As expected, the geolocation offset is shown to have negligible effect on the distributions of precipitation occurrence and volume over the high-latitude ocean, aligning with the consistency between those variables only differing by the offset in Table 1 and Fig. 3. On the other hand, the CORRA calibration process in IMERG-GMI has a large effect on the distributions of precipitation occurrence and volume, with GPROF-CLIM better representing the occurrence and volume of intermediate and heavy GR precipitation rates while IMERG-GMI better captures the occurrence of light GR precipitation rates (Figs. 5a,c). The CORRA calibration process increases the occurrence and volume of light and heavy precipitation rates, while reducing the occurrence and volume of intermediate precipitation rates over the high-latitude ocean.

For the tropical ocean, the mode precipitation occurrence is ~0.04 mm h^{-1} for GPROF-CLIM and IMERG-GMI, while it is ~0.07 mm h^{-1} for the GRs (Fig. 6a). The maximum precipitation volume is ~0.23 mm h^{-1} for GPROF-CLIM, while it is ~0.4 mm h^{-1} for the GRs and IMERG-GMI. The geolocation offset has a minimal effect on the distributions of precipitation occurrence and volume over the tropical ocean, as evidenced by the similar distributions prior to and after correction of the offset for GPROF-CLIM and IMERG-GMI. The CORRA calibration process in IMERG-GMI acts to improve the precipitation occurrence and volume distributions relative to the GRs for the tropical ocean, unlike for the high-latitude ocean. Specifically, the CORRA calibration process decreases the occurrence and volume of light and intermediate precipitation rates and increases the occurrence and volume of heavy precipitation rates over the tropical ocean.

Overall, IMERG-GMI and GPROF-CLIM can capture the cumulative distributions of precipitation occurrence and volume over the tropical ocean, while only GPROF-CLIM can represent these distributions over the high-latitude ocean. IMERG-GMI's issues with biasing the cumulative precipitation occurrence and volume distributions toward higher precipitation rates over the high-latitude ocean compared to GPROF-CLIM is caused by the CORRA calibration procedure. Furthermore, these distribution results are consistent with the quantile-quantile lines shown in Figs. 3 and 4, where the IMERG-GMI quantile–quantile distribution is also strongly biased toward higher IMERG-GMI precipitation rates.

c. *Precipitation intensity variability*

One analysis that can help us to better understand the systematic and random errors in IMERG-GMI, and how these vary from the input GPROF-CLIM through the algorithm, is to determine the errors as a function of the precipitation intensity. Figures 7 and 8 depict the mean relative bias and random error for each satellite variable as a function of the GR precipitation rate for the high-latitude and tropical oceans, respectively.

Over the high-latitude ocean (Fig. 7), the CORRA calibration process clearly increases the mean relative bias and random error in IMERG-GMI while the V06B geolocation offset on the gridding of GPROF-CLIM footprints has minimal effect, as also identified in Table 1 and Fig. 3. GPROF-CLIM exhibits a near-perfect mean relative bias and low random error at heavy precipitation intensities, though strongly overestimates GR precipitation retrievals at light and intermediate precipitation intensities, with sharply increasing growth in bias and random error toward lighter rates. Error lines for IMERG-GMI show that the CORRA calibration process particularly exacerbates the errors at the heaviest precipitation rates ($R > 3$ mm h^{-1}), which corresponds with the density sample principally residing in the satellite overestimation domain at these precipitation rates in Figs. 3c and 3d.

Over the tropical ocean (Fig. 8), IMERG-GMI and GPROF-CLIM overestimate light and intermediate precipitation and underestimate the heaviest precipitation rates, similar to findings

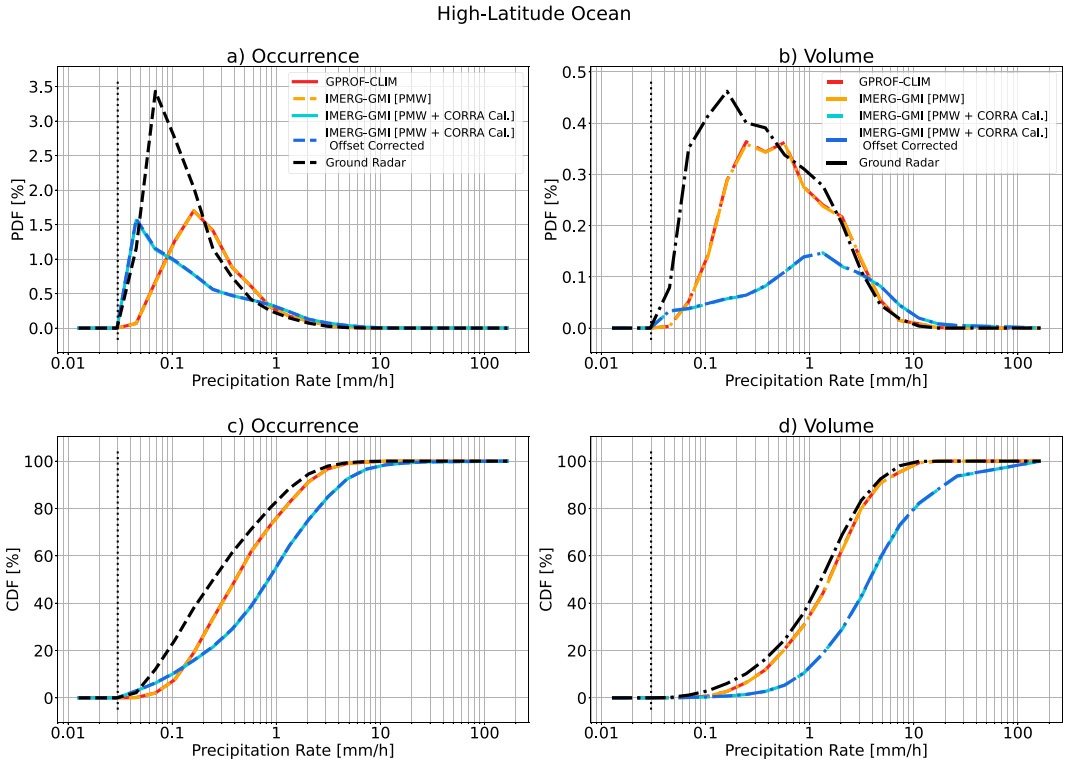

FIG. 5. Probability and cumulative density functions (PDFs and CDFs) of 0.1° × 0.1° gridded precipitation retrievals from IMERG V06B Final Run, GPROF-CLIM V05, and the reference GR over the high-latitude ocean. Results are restricted to GMI overpasses of the GRs in the period June 2014–August 2021 only. The density functions are for precipitation (left) occurrence and (right) amount, and the dotted line highlights the 0.03 mm h^{-1} rain–no rain threshold for this analysis. Each density function consists of 20 bins with their sizes increasing logarithmically between 0.01 and 300 mm h^{-1}, and each probability density value is weighted by the respective bin size. Note that the GPROF-CLIM (red) and IMERG-GMI [PMW + CORRA Cal.] (light blue) lines reside under the IMERG-GMI [PMW] (orange) and IMERG-GMI [PMW + CORRA Cal.]–Offset Corrected (dark blue) lines, respectively.

over land (Tan et al. 2016; O et al. 2017; Maranan et al. 2020; Kirstetter et al. 2020; Da Silva et al. 2021). IMERG-GMI and GPROF-CLIM exhibit exponential growth in mean relative bias and random error over tropical ocean, though this exponential growth starts in the heavy precipitation range unlike for the high-latitude ocean. The CORRA calibration procedure in the IMERG algorithm has minimal impact on the bias and random error trends over the tropical ocean, as also evidenced in Table 1 and Fig. 4. On the other hand, the geolocation offset has a large effect at intermediate precipitation rates for bias, and all but the heaviest precipitation rates ($R > 7$ mm h^{-1}) for random error.

Overall, IMERG-GMI typically better represents heavier precipitation regimes than lighter regimes, with lower mean relative biases and random errors. At lighter oceanic precipitation intensities ($R < 0.1$ mm h^{-1}), IMERG-GMI typically overestimates by >100%.

5. Discussion

This validation study is designed to identify where the IMERG algorithm can be improved in future versions, and ultimately to aid IMERG in providing the best possible representation of global precipitation. To put the results of this study into the context of IMERG's representation of global precipitation, Fig. 9 depicts the oceanic zonal mean precipitation from all GPM V06 products, as well as the GPCP V2.3 product, for the study period June 2014–August 2021; note that GPROF and GPROF-CLIM V05 are the products used in the GPM V06 product suite, and that the multisatellite IMERG product (and not IMERG-GMI) is shown. IMERG and GPROF-CLIM exhibit strong agreement for tropical oceanic mean precipitation, and the results of this validation study identify this agreement while also suggesting that IMERG and GPROF-CLIM means are +12% and +14% higher, respectively, than retrieved from ground sensors (Table 1). The agreement in zonal precipitation between the suite of GPM and GPCP products is restricted to the tropics, with differences between IMERG and GPROF-CLIM (as well as the other GPM-CO products) increasing at higher latitudes. At the latitude of Alaska's Middleton Island (59.5°N), IMERG's zonal mean precipitation is a factor of ~1.67 larger than that from GPROF-CLIM due primarily to the PMW calibration step in the IMERG algorithm, whereby the GPROF-CLIM retrievals are intercalibrated to CORRA (which is first climatologically adjusted to GPCP in

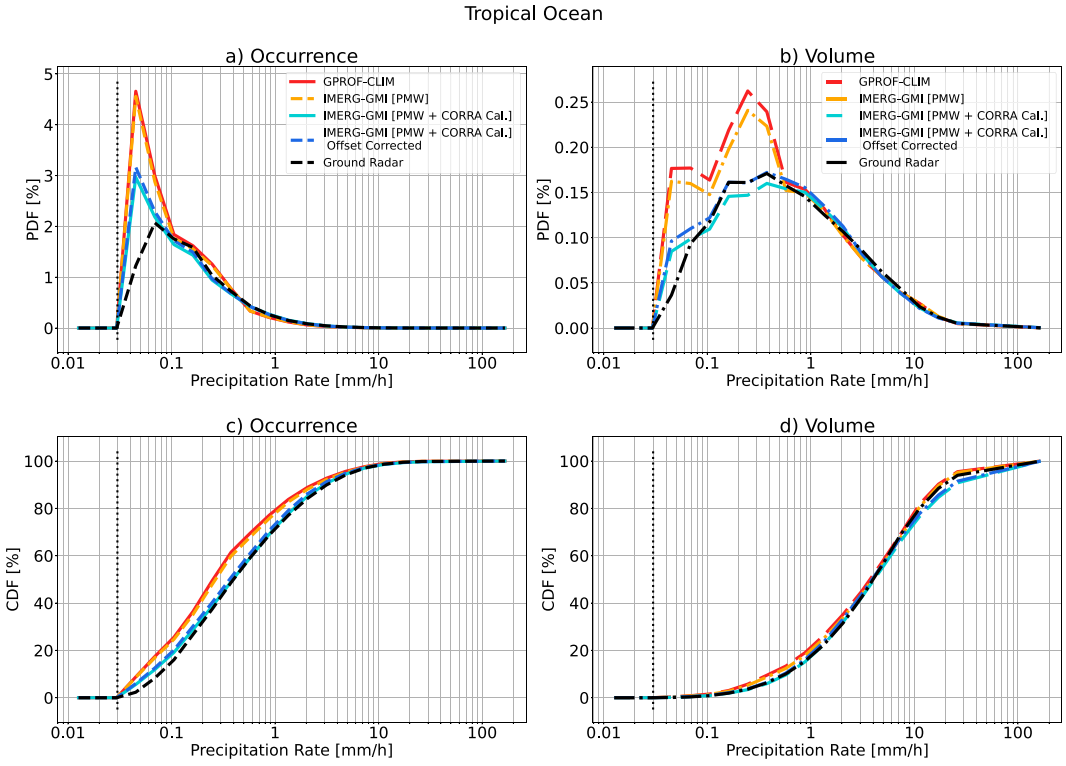

FIG. 6. As in Fig. 5, but for the tropical ocean. Note that the GPROF-CLIM (red) and IMERG-GMI [PMW + CORRA Cal.] (light blue) lines reside under the IMERG-GMI [PMW] (orange) and IMERG-GMI [PMW + CORRA Cal.]–Offset Corrected (dark blue) lines, respectively, in some instances.

the IMERG algorithm). In this study, we have shown that the enhancement of high-latitude oceanic precipitation by IMERG's PMW calibration scheme acts to strongly increase the overestimating systematic error in the Gulf of Alaska, as evidenced by GPROF-CLIM and IMERG-GMI having mean relative biases of +15% and +147%, respectively.

The increase in IMERG's oceanic zonal mean precipitation at high latitudes appears to be driven by the GPCP component in the PMW calibration scheme, and not CORRA, as expected. This is evident from the close agreement between IMERG and GPCP at high latitudes, while CORRA is nearly a factor of ~2 smaller than both products, highlighting that the GPCP adjustment to CORRA in IMERG's PMW calibration process increases precipitation estimates over high-latitude ocean (section 2a). Our future studies will further trace IMERG errors by assessing GPCP to identify the cause of such large amounts of high-latitude precipitation. We know that gauge estimates are not the cause for this as they do not contribute to any oceanic retrievals in GPCP V2.3 or IMERG V06B. Continuing to trace errors back through multisatellite precipitation algorithms is key to their improvement (Kirstetter et al. 2020).

A caveat of any validation study is that GR data, while considered a reference dataset, does not provide the absolute ground truth (Kirstetter et al. 2020, among many others). GR precipitation estimates have innate uncertainties caused by nonuniform beam filling, radar calibration, radar beam resolution, radar signal attenuation, and retrieval of surface precipitation from elevated scans (Cifelli et al. 2011). The CSU-HIDRO GR retrievals used in this study have robust performance in tropical and midlatitude regions, though exhibit high sensitivity to the dual-polarization thresholds selected (Cifelli et al. 2011). Also, at low reflectivities, CSU-HIDRO relies on the relationship between reflectivity and rain rate, which can exhibit considerable variability due to differing drop size distributions (Ulbrich and Atlas 1998). Consideration should also be taken that the GRs used in this study mainly reside on islands, and consequently may not be fully representative of the open ocean water due to coastline effects on the diurnal cycle of precipitation (Watters et al. 2021).

The high-latitude ocean results in this analysis are restricted to one GR located on Alaska's Middleton Island. These results cannot be considered representative of the entire high-latitude ocean domain and are likely affected by the lack of longitudinal variation in the GPCP zonal-mean adjustment applied to IMERG. The acquisition of data from further GRs at high latitudes in coastal and/or island regions would be of benefit to the precipitation community for further studies and could detail how representative our Middleton Island oceanic results are relative to other high-latitude oceanic domains such as in the Southern Hemisphere.

The tropical ocean results are aggregated from five different GRs, though the individual GRs generally agree that the geolocation offset has a larger impact on IMERG-GMI performance than the PMW calibration scheme. Some tropical

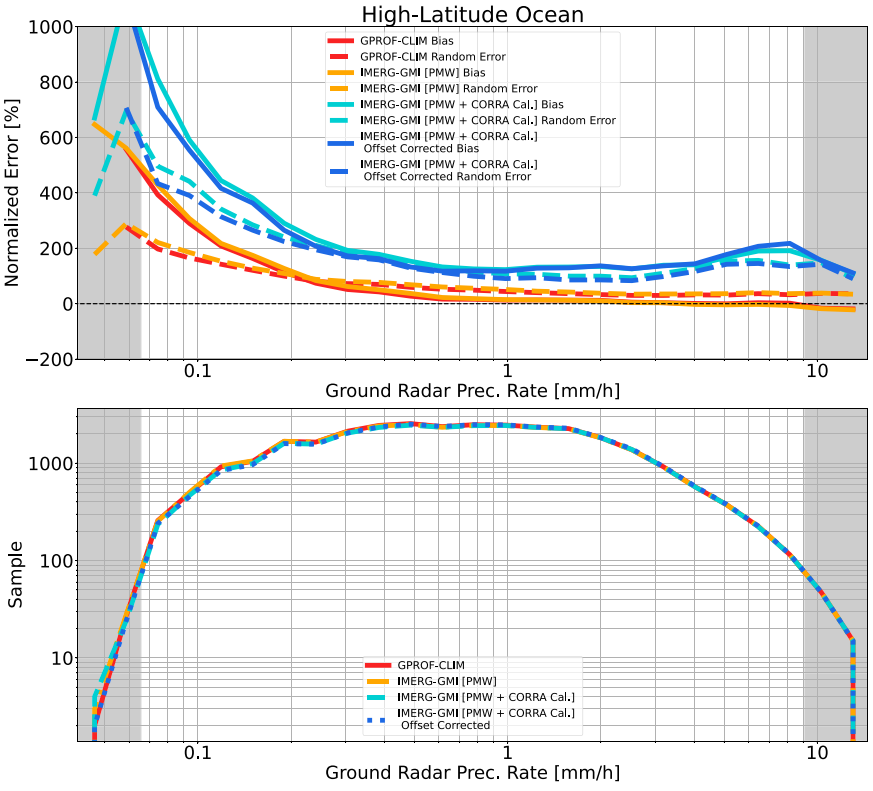

FIG. 7. The mean relative bias (solid lines) and random error (dashed lines) as a function of GR precipitation intensity for gridded IMERG V06B Final Run and GPROF-CLIM V05 precipitation retrievals over the high-latitude ocean. Results are restricted to GMI overpasses of the GRs in the period June 2014–August 2021 only. (top) Systematic and random errors, and (bottom) the corresponding sample size per GR precipitation rate bin. Shaded regions depict where the sample size is less than 100 grid boxes, and hence results there are considered unreliable.

ocean results differ between individual sites; i.e., GPROF-CLIM and IMERG-GMI underestimate oceanic precipitation close to the Puerto Rican GR (TJUA) while the products overestimate close to the other tropical GRs and in the aggregated results. Aggregated tropical oceanic results are favored in this analysis due to the varying and small sample sizes of the individual GRs.

Future validation studies with the GPM VN will benefit from updates to the suite of GPM matchup products. In particular, the GR estimates at the satellite footprint scale will be determined from the estimates in the whole field of view rather than just the precipitating region (switching from conditional to unconditional precipitation rates). This advancement will better represent the GR estimates of the precipitation field for the satellite footprint, particularly at light rates. Including nonprecipitating regions within the mean GR estimate for the satellite footprint is expected to reduce the GR precipitation rates, which in turn will likely enhance the overestimating IMERG and GPROF-CLIM biases quantified in this study.

The results of this study build on previous oceanic validation works. Like the Pacific Ocean results from Bolvin et al. (2021), IMERG is identified to have a small overestimating oceanic bias over the tropics, although the mean relative bias of +0.67% identified in their study is smaller than identified in our study (+12%). Furthermore, at first glance their IMERG Pacific Ocean correlation of 0.68 seems superior to the tropical ocean correlation of 0.42 identified here. However, reduced biases and improved correlations are likely driven by their evaluation of monthly data rather than half-hourly, with other factors including their investigation of a different oceanic location, use of a set of gauges rather than GRs, and inclusion of other PMW constellation members and IMERG algorithm steps (PMW morphing, inclusion of IR estimates, etc.) whereas this study is restricted to GMI only. Wang et al. (2022) assessed IMERG V06 using the S-band weather GR on the Kwajalein Atoll (KPOL) in the period 2014–18, identifying an underestimating bias by IMERG of −9%. Our study includes KWAJ in the tropical ocean cluster of radars, with our KWAJ results identifying a smaller bias of 0%. The smaller bias in our study may be due to the IMERG analysis being restricted to GMI only, whereas that of Wang et al. (2022) considered all PMW, IR and morphing components of the IMERG algorithm. A smaller bias from the GMI compared to the suite of multisatellite components in IMERG is not unexpected as the GMI is the highest-quality sensor contributing to IMERG.

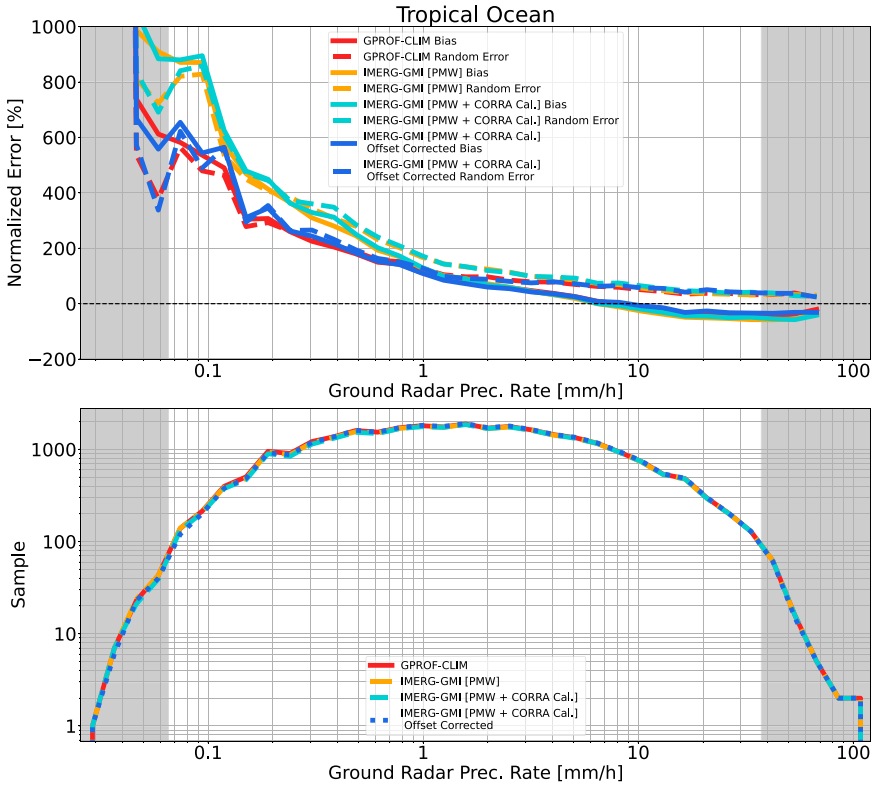

FIG. 8. As in Fig. 7, but for the tropical ocean.

The results of the present study document important features of V06 for current application users and act as a benchmark for assessing V07 upgrades, including the impact of the upgraded Kalman filter. We plan future V07 studies to stratify IMERG errors by hydrometeor classification and homogeneity of the precipitation field using the novelties of the GPM VN.

6. Conclusions

This study has evaluated the performance of NASA's global-gridded precipitation product, IMERG V06B Final Run, in representing precipitation at instances of GMI overpasses (i.e., IMERG-GMI) over high-latitude and tropical oceans between June 2014 and August 2021. In this analysis, we have assessed IMERG-GMI using the GPM Validation Network (VN), which provides ground radar (GR) retrievals matched to the GPROF GMI footprint scale (10.9 km × 18.1 km). GR sites in this analysis include one high-latitude site on Alaska's Middleton Island, and five tropical island sites: Hawaii's Kauai (PHKI) and Molokai (PHMO) islands, Puerto Rico (TJUA), Guam (PGUA), and the Kwajalein Atoll (KWAJ) (Fig. 1). We have enabled a novel error tracing assessment throughout the IMERG algorithm by gridding the GPROF GMI climate product (GPROF-CLIM) and GR precipitation retrievals from the GPROF footprint scale to the 0.1° × 0.1° grid using the IMERG backward gridding technique. This error tracing technique has allowed us to assess the impact of IMERG's V06B geolocation offset error, whereby GPROF-CLIM footprints are incorrectly offset by 0.1° eastward (discussed in section 2a), and the passive microwave (PMW) calibration procedure applied by IMERG to the GPROF-CLIM GMI estimates input to the algorithm. We only assessed IMERG performance for the GMI sensor because 1) the GMI is the calibration standard in the GPM PMW satellite constellation and should provide the best performance of all sources in the multisatellite IMERG product, and 2) the GPM VN only provides GR to GPROF matchups for the GMI sensor, hence the GMI is the only source for which a full error tracing analysis through the IMERG algorithm can be performed.

The main results of this analysis are as follows:

1) The IMERG V06B gridder incorrectly geolocates GPROF-CLIM PMW footprint estimates by 0.1° eastward, and the gridded CORRA calibrations by 0.025° eastward, in the latitude range 75°N–75°S. This affects IMERG V06B and all earlier versions and has been corrected in IMERG V07.
2) IMERG-GMI V06B overestimates precipitation over the Alaskan high-latitude ocean by +147%, and overestimates precipitation over the tropical ocean by +12% (Table 1).
3) Over the Alaskan high-latitude ocean, the PMW calibration procedure has a detrimental effect on the accuracy of IMERG-GMI estimates as it increases both the systematic and random errors from the input GPROF-CLIM V05 product (i.e., mean relative bias increases from +15% to +147%, random error increases from 41% to

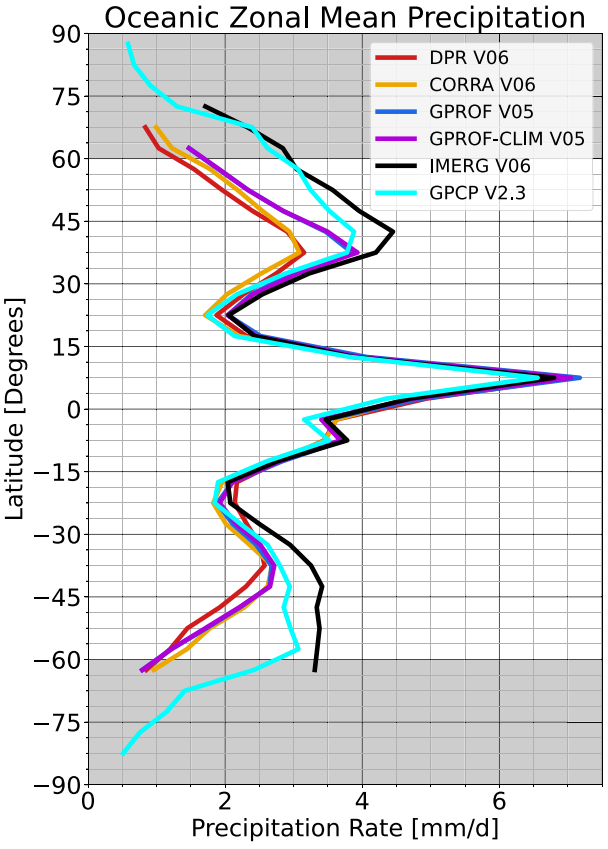

FIG. 9. Oceanic zonal mean precipitation from GPM and GPCP products in the period June 2014–August 2021. The GPM V06 suite includes the GPM-CO DPR, CORRA [DPR + GMI], GPROF [GMI-only], and GPROF-CLIM [GMI-only] products and the multisatellite IMERG product; note that there is no V06 of GPROF and GPROF-CLIM, and GPROF-CLIM V05 is the input to IMERG V06B. GPCP V2.3 provides the climatological calibration to CORRA V06, which in turn calibrates GPROF-CLIM V05 (for all PMW sensors) within the IMERG algorithm.

154%). Correcting for the IMERG V06B geolocation offset slightly improves the systematic and random errors, though the impact is minimal compared to the PMW calibration process (Fig. 3).

4) Over the tropical ocean, the PMW calibration procedure in IMERG-GMI V06B has minimal impact on the systematic and random errors, whereas the V06B geolocation offset error has a larger impact on the errors (i.e., mean absolute bias increases from 73% to 89%, random error increases from 71% to 89%, correlation decreases from 0.61 to 0.45; Fig. 4).
5) IMERG-GMI V06B and GPROF-CLIM V05 have skill in capturing the precipitation occurrence and volume distributions over the tropical ocean, though IMERG-GMI V06B does not possess such skill over the Alaskan high-latitude ocean (Figs. 5 and 6). The PMW calibration procedure in IMERG-GMI V06B redistributes GPROF-CLIM V05 precipitation by biasing the distributions of occurrence and volume toward higher precipitation rates over the high-latitude ocean.
6) IMERG-GMI V06B typically has lower systematic and random errors for heavier precipitation regimes than lighter regimes over ocean (Figs. 7 and 8). IMERG-GMI V06B typically overestimates lighter oceanic precipitation ($R < 0.1$ mm h^{-1}) by >100%.

This novel IMERG validation study fully traces errors back through the algorithm for the first time. These findings will aid in improving the algorithm design for IMERG V08, likely by informing how to apply the GPCP-combined PMW calibration scheme in light of persistent high-latitude oceanic biases. Furthermore, these findings will inform GPROF about its oceanic precipitation biases, which in turn will benefit IMERG. Future work will be conducted to assess the GPCP-combined PMW calibration scheme in IMERG in greater detail. In particular, the GPCP product will be assessed using the GPM VN as it appears that it is this component of IMERG's PMW calibration scheme, and not the GPM CORRA component, which drives the overestimation in IMERG-GMI's high-latitude oceanic precipitation (Fig. 9). Other future work will assess the IMERG V07 product to see whether the algorithm updates improve its performance relative to V06.

Acknowledgments. Daniel Watters was supported by an appointment to the NASA Postdoctoral Program at NASA Marshall Space Flight Center, administered by Oak Ridge Associated Universities under contract with NASA. Patrick Gatlin, David Bolvin, George Huffman, Robert Joyce, Eric Nelkin, and Jackson Tan were supported by the NASA Precipitation Measurement Missions funding (program manager Will McCarty), including WBSs 378289.04.08.01 and 573945.04.80.01.01. Pierre Kirstetter was funded by the NASA Global Precipitation Measurement Ground Validation program under Grant 80NSSC21K2045 and the Precipitation Measurement Missions program under Grant 80NSSC19K0681. We thank Francisco Tapiador and two other anonymous reviewers for their helpful comments and recommendations which improved the paper. We thank Todd Berendes and Denise Berendes (University of Alabama in Huntsville) and Jason Pippitt (Science Systems and Applications Inc.; NASA GSFC) for their work in upgrading the GPM VN files and the GPM Ground Validation System files, respectively, and Chris Kummerow (Colorado State University) for providing information on GPROF.

Data availability statement. The IMERG V06B Final Run, GPROF V05, and GPM Validation Network GRtoGPROF V2.3 datasets used in this analysis are freely available from Huffman et al. (2019a), Kummerow (2017), and NASA (2023), respectively. Furthermore, the DPR V06, CORRA V06, and GPCP V2.3 datasets used in the zonal comparison are freely available from Iguchi and Meneghini (2017), Olson (2017), and Adler et al. (2016), respectively.

REFERENCES

Adler, R., and Coauthors, 2016: Global Precipitation Climatology Project (GPCP) Climate Data Record (CDR), version 2.3.

National Centers for Environmental Information, accessed 13 March 2023, https://doi.org/10.7289/V56971M6.

Adler, R. F., and Coauthors, 2003: The version-2 Global Precipitation Climatology Project (GPCP) monthly precipitation analysis (1979–present). *J. Hydrometeor.*, **4**, 1147–1167, https://doi.org/10.1175/1525-7541(2003)004<1147:TVGPCP>2.0.CO;2.

——, and Coauthors, 2018: The Global Precipitation Climatology Project (GPCP) monthly analysis (new version 2.3) and a review of 2017 global precipitation. *Atmosphere*, **9**, 138, https://doi.org/10.3390/atmos9040138.

Battaglia, A., K. Mroz, D. Watters, and F. Ardhuin, 2019: GPM-derived climatology of attenuation due to clouds and precipitation at Ka-band. *IEEE Trans. Geosci. Remote Sens.*, **58**, 1812–1820, https://doi.org/10.1109/TGRS.2019.2949052.

Berg, W., and Coauthors, 2016: Intercalibration of the GPM microwave radiometer constellation. *J. Atmos. Oceanic Technol.*, **33**, 2639–2654, https://doi.org/10.1175/JTECH-D-16-0100.1.

Bogerd, L., A. Overeem, H. Leijnse, and R. Uijlenhoet, 2021: A comprehensive five-year evaluation of IMERG late run precipitation estimates over the Netherlands. *J. Hydrometeor.*, **22**, 1855–1868, https://doi.org/10.1175/JHM-D-21-0002.1.

Bolvin, D. T., G. J. Huffman, E. J. Nelkin, and J. Tan, 2021: Comparison of monthly IMERG precipitation estimates with PACRAIN atoll observations. *J. Hydrometeor.*, **22**, 1745–1753, https://doi.org/10.1175/JHM-D-20-0202.1.

Bytheway, J. L., E. J. Thompson, J. Yang, and H. Chen, 2023: Evaluating satellite precipitation estimates over oceans using passive aquatic listeners. *Geophys. Res. Lett.*, **50**, e2022GL102087, https://doi.org/10.1029/2022GL102087.

Cifelli, R., V. Chandrasekar, S. Lim, P. C. Kennedy, Y. Wang, and S. A. Rutledge, 2011: A new dual-polarization radar rainfall algorithm: Application in Colorado precipitation events. *J. Atmos. Oceanic Technol.*, **28**, 352–364, https://doi.org/10.1175/2010JTECHA1488.1.

Da Silva, N. A., B. G. M. Webber, A. J. Matthews, M. M. Feist, T. H. M. Stein, C. E. Holloway, and M. F. A. B. Abdullah, 2021: Validation of GPM IMERG extreme precipitation in the Maritime Continent by station and radar data. *Earth Space Sci.*, **8**, e2021EA001738, https://doi.org/10.1029/2021EA001738.

Derin, Y., and P.-E. Kirstetter, 2022: Evaluation of IMERG over CONUS complex terrain using environmental variables. *Geophys. Res. Lett.*, **49**, e2022GL100186, https://doi.org/10.1029/2022GL100186.

——, ——, and J. J. Gourley, 2021: Evaluation of IMERG satellite precipitation over the land–coast–ocean continuum. Part I: Detection. *J. Hydrometeor.*, **22**, 2843–2859, https://doi.org/10.1175/JHM-D-21-0058.1.

——, ——, N. Brauer, J. J. Gourley, and J. Wang, 2022: Evaluation of IMERG satellite precipitation over the land–coast–ocean continuum. Part II: Quantification. *J. Hydrometeor.*, **23**, 1297–1314, https://doi.org/10.1175/JHM-D-21-0234.1.

Gatlin, P. N., W. A. Petersen, J. L. Pippitt, T. A. Berendes, D. B. Wolff, and A. Tokay, 2020: The GPM validation network and evaluation of satellite-based retrievals of the rain drop size distribution. *Atmosphere*, **11**, 1010, https://doi.org/10.3390/atmos11091010.

Gowan, T. A., and J. D. Horel, 2020: Evaluation of IMERG-E precipitation estimates for fire weather applications in Alaska. *Wea. Forecasting*, **35**, 1831–1843, https://doi.org/10.1175/WAF-D-20-0023.1.

Hayden, L., and C. Liu, 2021: Differences in the diurnal variation of precipitation estimated by spaceborne radar, passive microwave radiometer, and IMERG. *J. Geophys. Res. Atmos.*, **126**, e2020JD033020, https://doi.org/10.1029/2020JD033020.

Hayden, L. J. M., J. Tan, D. T. Bolvin, and G. J. Huffman, 2023: Variations in the diurnal cycle of precipitation and its changes with distance from shore over two contrasting regions as observed by IMERG, ERA5, and spaceborne Ku radar. *J. Hydrometeor.*, **24**, 675–689, https://doi.org/10.1175/JHM-D-22-0154.1.

Hou, A. Y., and Coauthors, 2014: The Global Precipitation Measurement mission. *Bull. Amer. Meteor. Soc.*, **95**, 701–722, https://doi.org/10.1175/BAMS-D-13-00164.1.

Huffman, G. J., E. Stocker, D. Bolvin, E. Nelkin, and J. Tan, 2019a: GPM IMERG final precipitation L3 half hourly 0.1 degree × 0.1 degree, V06 (GPM_3IMERGHH). Goddard Earth Sciences Data and Information Services Center (GES DISC), accessed 13 March 2023, https://doi.org/10.5067/GPM/IMERG/3B-HH/06.

——, and Coauthors, 2019b: NASA Global Precipitation Measurement (GPM) Integrated Multi-satellitE Retrievals for GPM (IMERG). Algorithm Theoretical Basis Doc., version 6. 38 pp., https://pmm.nasa.gov/sites/default/files/document_files/IMERG_ATBD_V06.pdf.

——, D. T. Bolvin, E. J. Nelkin, E. F. Stocker, and J. Tan, 2020a: V06 IMERG release notes. NASA Tech. Rep., 15 pp., https://gpm.nasa.gov/sites/default/files/2020-10/IMERG_V06_release_notes_201006_0.pdf.

——, and Coauthors, 2020b: Integrated multi-satellite retrievals for the Global Precipitation Measurement (GPM) mission (IMERG). *Satellite Precipitation Measurement*, Springer, 343–353, https://doi.org/10.1007/978-3-030-24568-9_19.

Iguchi, T., and R. Meneghini, 2017: GPM DPR Precipitation Profile, Version 6. Goddard Earth Sciences Data and Information Services Center (GES DISC), accessed 13 March 2023, https://arthurhouhttps.pps.eosdis.nasa.gov/gpmallversions/V06/YYYY/MM/DD/radar.

——, and Coauthors, 2018: GPM/DPR Level-2. Algorithm Theoretical Basis Doc., 127 pp., https://pps.gsfc.nasa.gov/Documents/ATBD_DPR_201811_with_Appendix3b.pdf.

Joyce, R. J., and P. Xie, 2011: Kalman filter–based CMORPH. *J. Hydrometeor.*, **12**, 1547–1563, https://doi.org/10.1175/JHM-D-11-022.1.

——, J. E. Janowiak, P. A. Arkin, and P. Xie, 2004: CMORPH: A method that produces global precipitation estimates from passive microwave and infrared data at high spatial and temporal resolution. *J. Hydrometeor.*, **5**, 487–503, https://doi.org/10.1175/1525-7541(2004)005<0487:CAMTPG>2.0.CO;2.

Khan, S., and V. Maggioni, 2019: Assessment of Level-3 Gridded Global Precipitation Mission (GPM) products over oceans. *Remote Sens.*, **11**, 255, https://doi.org/10.3390/rs11030255.

Kidd, C., Y. N. Takayabu, G. M. Skofronick-Jackson, G. J. Huffman, S. A. Braun, T. Kubota, and F. J. Turk, 2020: The Global Precipitation Measurement (GPM) mission. *Satellite Precipitation Measurement*, Springer, 3–23, https://doi.org/10.1007/978-3-030-24568-9_1.

Kirschbaum, D. B., and Coauthors, 2017: NASA's remotely sensed precipitation: A reservoir for applications users. *Bull. Amer. Meteor. Soc.*, **98**, 1169–1184, https://doi.org/10.1175/BAMS-D-15-00296.1.

Kirstetter, P.-E., W. A. Petersen, C. D. Kummerow, and D. B. Wolff, 2020: Integrated multi-satellite evaluation for the Global Precipitation Measurement: Impact of precipitation types on spaceborne precipitation estimation. *Satellite Precipitation Measurement*, Springer, 583–608, https://doi.org/10.1007/978-3-030-35798-6_7.

Kummerow, C., 2017: GPM GMI (GPROF) climate-based radiometer precipitation profiling, version 5. Goddard Earth Sciences Data and Information Services Center (GES DISC), accessed 13 March 2023, https://arthurhouhttps.pps.eosdis.nasa.gov/gpmallversions/V05/YYYY/MM/DD/gprof.

——, W. Barnes, T. Kozu, J. Shiue, and J. Simpson, 1998: The Tropical Rainfall Measuring Mission (TRMM) sensor package. *J. Atmos. Oceanic Technol.*, **15**, 809–817, https://doi.org/10.1175/1520-0426(1998)015<0809:TTRMMT>2.0.CO;2.

——, D. L. Randel, M. Kulie, N.-Y. Wang, R. Ferraro, S. Joseph Munchak, and V. Petkovic, 2015: The evolution of the Goddard profiling algorithm to a fully parametric scheme. *J. Atmos. Oceanic Technol.*, **32**, 2265–2280, https://doi.org/10.1175/JTECH-D-15-0039.1.

Li, X., S. O, N. Wang, L. Liu, and Y. Huang, 2021: Evaluation of the GPM IMERG V06 products for light rain over Mainland China. *Atmos. Res.*, **253**, 105510, https://doi.org/10.1016/j.atmosres.2021.105510.

Mahmoud, M. T., S. A. Mohammed, M. A. Hamouda, M. Dal Maso, and M. M. Mohamed, 2021: Performance of the IMERG precipitation products over high-latitudes region of Finland. *Remote Sens.*, **13**, 2073, https://doi.org/10.3390/rs13112073.

Maranan, M., A. H. Fink, P. Knippertz, L. K. Amekudzi, W. A. Atiah, and M. Stengel, 2020: A process-based validation of GPM IMERG and its sources using a mesoscale rain gauge network in the West African forest zone. *J. Hydrometeor.*, **21**, 729–749, https://doi.org/10.1175/JHM-D-19-0257.1.

NASA, 2022: NASA Global Precipitation Measurement (GPM) Goddard Profiling (GPROF) Algorithm. Algorithm Theoretical Basis Doc., 62 pp., https://gpm.nasa.gov/sites/default/files/2022-06/ATBD_GPM_V7_GPROF.pdf.

——, 2023: GPM validation network V2.3 GRtoGPROF data. NASA Marshall Space Flight Center, accessed 10 March 2023, https://pmm-gv.gsfc.nasa.gov/pub/gpm-validation/data/gpmgv/netcdf/geo_match/GPM/GMI/2AGPROF/V07A/2_3/.

NASA-GSFC, 2015: Validation network data product user's guide: Volume 2 – GPM data products. NASA Tech. Rep., 107 pp., https://gpm.nasa.gov/sites/default/files/document_files/Val_Network_Users_Guide_Vol_2_Nov2015.pdf.

Nascimento, J. G., D. Althoff, H. C. Bazame, C. M. U. Neale, S. N. Duarte, A. L. Ruhoff, and I. Z. Gonçalves, 2021: Evaluating the latest IMERG products in a subtropical climate: The case of Paraná State, Brazil. *Remote Sens.*, **13**, 906, https://doi.org/10.3390/rs13050906.

Navarro, A., E. García-Ortega, A. Merino, J. L. Sánchez, C. Kummerow, and F. J. Tapiador, 2019: Assessment of IMERG precipitation estimates over Europe. *Remote Sens.*, **11**, 2470, https://doi.org/10.3390/rs11212470.

O, S., and P. Kirstetter, 2018: Evaluation of diurnal variation of GPM IMERG-derived summer precipitation over the contiguous US using MRMS data. *Quart. J. Roy. Meteor. Soc.*, **144**, 270–281, https://doi.org/10.1002/qj.3218.

——, U. Foelsche, G. Kirchengast, J. Fuchsberger, J. Tan, and W. A. Petersen, 2017: Evaluation of GPM IMERG early, late, and final rainfall estimates using WegenerNet gauge data in southeastern Austria. *Hydrol. Earth Syst. Sci.*, **21**, 6559–6572, https://doi.org/10.5194/hess-21-6559-2017.

Olson, W., 2017: GPM DPR and GMI combined precipitation. Goddard Earth Sciences Data and Information Services Center (GES DISC), accessed 13 March 2023, https://arthurhouhttps.pps.eosdis.nasa.gov/gpmallversions/V06/YYYY/MM/DD/radar.

——, 2022: GPM combined radar-radiometer precipitation Algorithm Theoretical Basis Document (version 6). NASA Tech. Rep., 94 pp., https://gpm.nasa.gov/sites/default/files/2023-01/Combined_algorithm_ATBD.V07_0.pdf.

Petersen, W. A., P.-E. Kirstetter, J. Wang, D. B. Wolff, and A. Tokay, 2020: The GPM ground validation program. *Satellite Precipitation Measurement*, Springer, 471–502.

Pippitt, J. L., D. B. Wolff, W. Petersen, and D. A. Marks, 2015: Data and operational processing for NASA's GPM ground validation program. *37th Conf. on Radar Meteorology*, Norman, OK, Amer. Meteor. Soc., 111, https://ams.confex.com/ams/37RADAR/webprogram/Handout/Paper275627/37radarposterpippitt.pdf.

Portier, A., D. Kirschbaum, M. Gebremichael, E. Kemp, S. Kumar, I. Llabres, E. Snodgrass, and J. Wegiel, 2023: NASA's Global Precipitation Measurement mission: Leveraging stakeholder engagement & applications activities to inform decision-Making. *Remote Sens. Appl. Environ.*, **29**, 100853, https://doi.org/10.1016/j.rsase.2022.100853.

Pradhan, R. K., and Coauthors, 2022: Review of GPM IMERG performance: A global perspective. *Remote Sens. Environ.*, **268**, 112754, https://doi.org/10.1016/j.rse.2021.112754.

Prakash, S., M. Ramesh Kumar, S. Mathew, and R. Venkatesan, 2018: How accurate are satellite estimates of precipitation over the North Indian Ocean? *Theor. Appl. Climatol.*, **134**, 467–475, https://doi.org/10.1007/s00704-017-2287-2.

Rajagopal, M., E. Zipser, G. Huffman, J. Russell, and J. Tan, 2021: Comparisons of IMERG version 06 precipitation at and between passive microwave overpasses in the tropics. *J. Hydrometeor.*, **22**, 2117–2130, https://doi.org/10.1175/JHM-D-20-0226.1.

Ramsauer, T., T. Weiß, and P. Marzahn, 2018: Comparison of the GPM IMERG final precipitation product to RADOLAN weather radar data over the topographically and climatically diverse Germany. *Remote Sens.*, **10**, 2029, https://doi.org/10.3390/rs10122029.

Randel, D. L., C. D. Kummerow, and S. Ringerud, 2020: The Goddard profiling (GPROF) precipitation retrieval algorithm. *Satellite Precipitation Measurement*, Springer, 141–152, https://doi.org/10.1007/978-3-030-24568-9_8.

Schneider, U., A. Becker, P. Finger, A. Meyer-Christoffer, M. Ziese, and B. Rudolf, 2014: GPCC's new land surface precipitation climatology based on quality-controlled in situ data and its role in quantifying the global water cycle. *Theor. Appl. Climatol.*, **115**, 15–40, https://doi.org/10.1007/s00704-013-0860-x.

Schwaller, M. R., and K. R. Morris, 2011: A ground validation network for the Global Precipitation Measurement mission. *J. Atmos. Oceanic Technol.*, **28**, 301–319, https://doi.org/10.1175/2010JTECHA1403.1.

Simpson, J., C. Kummerow, W.-K. Tao, and R. F. Adler, 1996: On the Tropical Rainfall Measuring Mission (TRMM). *Meteor. Atmos. Phys.*, **60**, 19–36, https://doi.org/10.1007/BF01029783.

Skofronick-Jackson, G., and Coauthors, 2017: The Global Precipitation Measurement (GPM) mission for science and society. *Bull. Amer. Meteor. Soc.*, **98**, 1679–1695, https://doi.org/10.1175/BAMS-D-15-00306.1.

——, D. Kirschbaum, W. Petersen, G. Huffman, C. Kidd, E. Stocker, and R. Kakar, 2018: The Global Precipitation Measurement (GPM) mission's scientific achievements and societal contributions: Reviewing four years of advanced rain and snow observations. *Quart. J. Roy. Meteor. Soc.*, **144**, 27–48, https://doi.org/10.1002/qj.3313.

Tan, J., W. A. Petersen, and A. Tokay, 2016: A novel approach to identify sources of errors in IMERG for GPM ground validation. *J. Hydrometeor.*, **17**, 2477–2491, https://doi.org/10.1175/JHM-D-16-0079.1.

——, G. J. Huffman, D. T. Bolvin, and E. J. Nelkin, 2019a: Diurnal cycle of IMERG V06 precipitation. *Geophys. Res. Lett.*, **46**, 13 584–13 592, https://doi.org/10.1029/2019GL085395.

——, ——, ——, and ——, 2019b: IMERG V06: Changes to the morphing algorithm. *J. Atmos. Oceanic Technol.*, **36**, 2471–2482, https://doi.org/10.1175/JTECH-D-19-0114.1.

——, ——, ——, ——, and M. Rajagopal, 2021: SHARPEN: A scheme to restore the distribution of averaged precipitation fields. *J. Hydrometeor.*, **22**, 2105–2116, https://doi.org/10.1175/JHM-D-20-0225.1.

Tapiador, F. J., A. Navarro, E. García-Ortega, A. Merino, J. L. Sánchez, C. Marcos, and C. Kummerow, 2020: The contribution of rain gauges in the calibration of the IMERG product: Results from the first validation over Spain. *J. Hydrometeor.*, **21**, 161–182, https://doi.org/10.1175/JHM-D-19-0116.1.

Trenberth, K. E., L. Smith, T. Qian, A. Dai, and J. Fasullo, 2007: Estimates of the global water budget and its annual cycle using observational and model data. *J. Hydrometeor.*, **8**, 758–769, https://doi.org/10.1175/JHM600.1.

Ulbrich, C. W., and D. Atlas, 1998: Rainfall microphysics and radar properties: Analysis methods for drop size spectra. *J. Appl. Meteor.*, **37**, 912–923, https://doi.org/10.1175/1520-0450(1998)037<0912:RMARPA>2.0.CO;2.

Wang, J., W. A. Petersen, D. B. Wolff, and G.-H. Ryu, 2020: Evaluation of GPM IMERG products over South Korea. *IGARSS 2020-2020 IEEE Int. Geoscience and Remote Sensing Symp.*, Waikoloa, HI, Institute of Electrical and Electronics Engineers, 5356–5359, https://doi.org/10.1109/IGARSS39084.2020.9323244.

——, ——, and ——, 2021: Validation of satellite-based precipitation products from TRMM to GPM. *Remote Sens.*, **13**, 1745, https://doi.org/10.3390/rs13091745.

——, D. B. Wolff, J. Tan, D. A. Marks, J. L. Pippitt, and G. J. Huffman, 2022: Validation of IMERG oceanic precipitation over Kwajalein. *Remote Sens.*, **14**, 3753, https://doi.org/10.3390/rs14153753.

Watters, D., and A. Battaglia, 2019: The summertime diurnal cycle of precipitation derived from IMERG. *Remote Sens.*, **11**, 1781, https://doi.org/10.3390/rs11151781.

——, and ——, 2021a: The NASA-JAXA Global Precipitation Measurement mission – Part I: New frontiers in precipitation. *Weather*, **76**, 41–44, https://doi.org/10.1002/wea.3865.

——, and ——, 2021b: The NASA-JAXA Global Precipitation Measurement mission – Part II: New frontiers in precipitation science. *Weather*, **76**, 52–56, https://doi.org/10.1002/wea.3869.

——, ——, and R. P. Allan, 2021: The diurnal cycle of precipitation according to multiple decades of global satellite observations, three CMIP6 models, and the ECMWF reanalysis. *J. Climate*, **34**, 5063–5080, https://doi.org/10.1175/JCLI-D-20-0966.1.

Wentz, F. J., and D. Draper, 2016: On-orbit absolute calibration of the Global Precipitation Measurement microwave imager. *J. Atmos. Oceanic Technol.*, **33**, 1393–1412, https://doi.org/10.1175/JTECH-D-15-0212.1.

You, Y., and Coauthors, 2021: Improving cross-track scanning radiometers' precipitation retrieval over ocean by morphing. *J. Hydrometeor.*, **22**, 2393–2406, https://doi.org/10.1175/JHM-D-21-0038.1.